Low Temperature Synthesis Route and Structural Characterization of $(Bi_{0.5}A_{0.5})(Sc_{0.5}Nb_{0.5})O_3$ (A = K^+ and Na^+) Perovskites

Journal:	*Inorganic Chemistry Frontiers*
Manuscript ID	QI-RES-02-2018-000144.R1
Article Type:	Research Article
Date Submitted by the Author:	17-Mar-2018
Complete List of Authors:	Surta, Todd; Oregon State University Manjon Sanz, Alicia; Oregon State University, Chemistry Qian, Eric; Oregon State University, Chemistry Tran, T. Thao; Johns Hopkins University, Chemistry Dolgos, Michelle; Oregon State University, Chemistry

Low Temperature Synthesis Route and structural characterization of $(Bi_{0.5}A_{0.5})(Sc_{0.5}Nb_{0.5})O_3$ ($A = K^+$ and Na^+) Perovskites

T. Wesley Surta[a], Alicia Manjón-Sanz[a], Eric Qian[a], T. Thao Tran[b], Michelle Dolgos[a*]

[a] Department of Chemistry, Oregon State University, Corvallis, OR, 97330, USA
[b] Department of Chemistry, University of Houston, Houston, TX, 77204, USA

Abstract

Two new perovskites, $(Bi_{0.5}A_{0.5})(Sc_{0.5}Nb_{0.5})O_3$ where $A = K^+$ and Na^+, have been made phase pure for the first time. The synthesis procedure that prevented the formation of pyrochlore impurities is described. *B*-site ordering in $A = K^+$ is successfully achieved by prolonged heating. Combined Rietveld refinement on synchrotron X-ray diffraction and neutron diffraction data is used to determine the complex average structure of these materials. $A = Na^+$ crystallizes in the tetragonal $P4/mbm$ space group and has disordered $a^oa^oc^+$ rotations of BO_6 octahedra. $A = K^+$ crystallizes in the cubic $Pm\bar{3}m$ space group, but shows local *A*-site displacements in the [100] direction. Both materials are highly disordered but illustrate the potential of $(A)NbO_3$-$BiScO_3$ solid solutions as useful piezoelectrics or relaxors.

Introduction

The perovskite structure is a family of materials with a general stoichiometry of ABX_3, where *A* is a large cation with 12-fold coordination, *B* is a smaller cation with 6-fold octahedral coordination, and *X* is an anion. This stoichiometry leads to an enormous amount of compositional flexibility where *X* anions include halogens, nitrogen, and oxygen, while *A* and *B* site cations include almost the entire periodic table and even some small molecules.[1–3] Perovskites are the most technologically relevant materials ever studied as they are used in applications such as superconductors, transparent conductors, ionic conductors, dielectrics, photovoltaic materials, piezoelectrics, ferroelectrics, and multiferroics.[3–10] Between the enormous compositional flexibility and diversity in properties it is clear why there is so much research interest in perovskites.

The ideal perovskite structure is simple, with the cubic aristotype, $Pm\bar{3}m$, being the highest symmetry space groups of this structure type. This simplicity quickly fades with compositional nuances. Depending on the composition, cations can displace, BX_6 octahedra can tilt, and both *B*-sites and *A*-sites can order in a variety of different patterns. This structural freedom allows perovskites to crystallize in a wide variety of space groups, with the difference between some structures being very subtle. The diversity and subtlety in structures makes the crystallography challenging at times, but allows for the rational tuning of properties. Perovskites have also inspired numerous group theoretical analyses, with the group theory even being extensively debated.[11,12] Well known perovskites have been studied for decades where compositions such as $NaNbO_3$, $BaTiO_3$ and $Pb(Zr_{1-x}Ti_x)O_3$, have structures that are still being investigated and revised today after decades of research.[13–17] To fully understand the interesting properties that many of these perovskites possess, these structural nuances must be fully understood.

One area that highlights the complexity of the perovskite structure is the study relaxor materials, a subset of ferroelectrics. Relaxors show a maximum in their dielectric permittivity at a temperature (T_m) that is frequency dependent. This frequency dependence coupled with the ferroelectric and piezoelectric properties make them useful electronic materials, in particular for actuator applications that require high strains.[18] Most relaxors appear to have a $Pm\bar{3}m$ structure, even when using high resolution synchrotron or neutron diffraction, which contradicts the structural requirements of ferroelectric materials having a non-centrosymmetric structure.[19] While a cubic-like average structure is observed in relaxors, their properties are derived from a complicated local structure due to the presence of polar nanoregions that align with an applied electric field. The pseudosymmetry of the long-range structure, where lattice parameters and atomic positions are metrically cubic, is common in relaxors. To fully understand and tune their interesting properties, the symmetry breaking distortions at the local level must be better understood.

In this work we synthesize two perovskite oxides, $(Bi_{0.5}A_{0.5})(Sc_{0.5}Nb_{0.5})O_3$, where $A = K^+$ or Na^+. This is the first time $A = Na^+$ has been reported in the literature and the first time either material has been made without impurities.[20,21] Synchrotron X-ray diffraction (XRD) and neutron powder diffraction (NPD) data are presented and the combined Rietveld analysis of these data is described. The crystal structures of these materials are determined for the first time and their structures are related to the potential relaxor properties previously reported for $A = K^+$.[21] The structure is then discussed in the context of other ferroelectric and relaxor materials such as $KNbO_3$, $NaNbO_3$, $BiScO_3$, ordered and disordered $Pb(Sc_{0.5}Nb_{0.5})O_3$ (PSN), and $(K_{0.5}Na_{0.5})NbO_3$-$BiScO_3$ (KNN-$BiScO_3$) solid solutions.

Experimental

Materials were synthesized using the modified mixed oxide synthesis technique commonly implemented for PSN.[22,23] A wolframite precursor, $ScNbO_4$, was first synthesized from stoichiometric amounts of Sc_2O_3 (Strem, 99.9%) and Nb_2O_5 (Strem, 99.5%) that were mixed with acetone and ground in an agate mortar and pestle. This wolframite precursor was then pressed into 13 mm disks and annealed at 1500°C for 2 h with a 5°C/min heating and cooling rate.

Bi_2O_3 (Strem, 99.9%) and K_2CO_3 (Alfa Aesar, 99%) or Na_2CO_3 (Strem, 99.5%) were weighed out with 1 wt% excess to maintain stoichiometry upon volatilization during heating. These starting materials were mixed with the wolframite precursor and ground with acetone in an agate mortar and pestle. The powders were micronized by planetary ball milling in 15 mL of ethanol with eight 10 mm yttria stabilized zirconia balls to increase reactivity. The powders were milled at 200 rpm for 24 cycles consisting of 10 min of milling and a 5 minute pause after which the cycle repeated in the reverse direction. Micronized powders were then pressed into 13 mm discs, placed in covered alumina crucibles, buried in Na_2CO_3 or K_2CO_3 sacrificial powder for $A = Na^+$ and K^+ respectively to further prevent volatilization of alkali ions. These disks were then annealed twice at 650 °C for 12 h with a heating and cooling rate of 5°C/min and intermittent grinding.

Excess cationic precursors (<1%) remaining in the samples were removed by washing under vacuum with 1 M nitric acid, followed by water, and acetone. These samples were then dried at 110 °C for 4 h to remove any remaining solvent. To ensure no structural changes occurred due to washing, the samples were tested for acid stability. To check for stability, powders were submerged in concentrated HNO_3 (~16 M) for 30 min, after which they were washed under vacuum with water and acetone and dried as previously specified. These powders were analyzed by lab XRD before and after the wash.

To order the *B*-site cations, phase pure samples of $A = K^+$ were pressed into 13 mm discs, placed in covered alumina crucibles, buried in K_2CO_3, and annealed at 650 °C for 100 h with a 5 °C/min heating and cooling rate. This process was repeated for 100 h, 200 h, and 300 h. The samples were acid washed using the previous procedure after annealing.

XRD data were collected using a Miniflex 600 diffractometer with Cu Kα radiation (λ = 1.541862 Å) and used to determine phase purity. All data were collected from 10 to 60°, with a scan rate of 0.12°/min, with the exception of data containing pyrochlore impurities which was scanned at 5°/min. Synchrotron XRD data were collected at beamline 11-BM of the Advanced Photon Source at Argonne National Laboratory.[24] To account for sample absorption, crushed powders were attached to the outside of a 0.8 mm Kapton capillary by mixing with vacuum grease and placed inside of 1.5 mm Kapton capillary. The capillaries were spun during measurements to increase sample averaging. Data were collected at room temperature over a 2θ range of 0.5 to 50° using λ = 0.459980 Å for 1 h.

NPD data were collected at the Spallation Neutron Source at Oak Ridge National Lab using the POWGEN diffractometer.[25] Approximately 5 g of powders were loaded into vanadium cans and measured at room temperature for 1 h using a center wavelength of 1.066 Å, covering a range of *d*-spacings from 0.30013 to 4.59539 Å.

Combined Rietveld refinements were performed on Synchrotron XRD and NPD data using Topas Academic.[26] A Chebychev polynomial with 6 terms was used to fit the background of both data sets and additional pseudo-voigt peaks were used for XRD data to model amorphous contributions to the background from the Kapton and vacuum grease. The profile of XRD data was fit with the Stephens' model to account for anisotropic microstrain.[27] Isotropic displacement parameters for different cations on the *A*-site or *B*-site as well as all oxygen displacement parameters were constrained together. Atomic positions for all *B*-site cations were constrained together for all fits. The occupancies of all sites were fixed to match the purposed stoichiometry. Neutron absorption (μR) for samples was accounted for in the refinements and estimated to be 0.0654 and 0.0624 for $A = Na^+$ and K^+ respectively, primarily due to absorption from Sc^{3+}.[28,29] For all samples the background, lattice parameters, peak profile, scale factor, atomic positions, isotropic displacement parameters, and μR were refined.

Second harmonic generation (SHG) measurements were performed on phase pure powders made from crushing pellets. A Kurtz nonlinear optical system equipped with a Nd:YAG laser (λ = 1064 nm) was used. Unsieved powders were placed in capillary tubes and no indexing fluid was used for measurements. Reflected SHG light (λ = 532 nm) was collected using a photomultiplier tube. A more detailed description of the experimental procedure can be found in other publications.[30]

Results & Discussion

Synthesis

Ivanov *et al.* reported the synthesis of $A = K^+$ in 2014.[21] However, when using their synthesis method both their study and ours resulted in a significant pyrochlore impurity, as shown in Figure 1. The synthesis procedure involved reacting $KNbO_3$ with Bi_2O_3 and Sc_2O_3 at 1000°C for 2 h and sintering at 1200 °C for 2 h. The synthesis of $A = Na^+$ was reported in a thesis by Knapp, but similar impurities can be seen.[20] In Knapp's procedure, primary oxides and carbonates were mixed, annealed at 950 °C, and sintered at 1050 °C. Due to the higher volatility of alkali metals compared to Bi^{3+}, the emergent pyrochlore phase is believed to be Bi_2ScNbO_7, though some substitution of alkali metals into the structure may be present.[31,32] We altered strategies for the synthesis procedure and used the wolframite precursor, $ScNbO_4$, which has been used in the synthesis of PSN to suppress the formation of pyrochlore phase.[33] Heating $A = K^+$ at 950 °C for 12 h with $ScNbO_4$ still resulted in the formation of pyrochlore impurities.

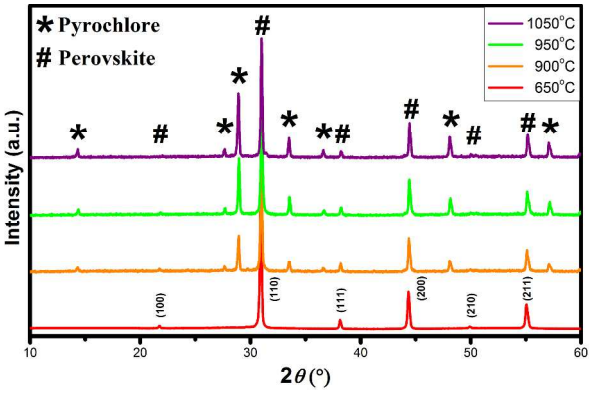

Figure 1. Lab XRD data for $A = K^+$ annealed at 650, 900, 950, and 1050 °C temperatures.

Synthesis at 1000°C and 1200°C is above the volatility temperature for alkali metals and above the annealing temperature for Bi_2ScNbO_7.[31,32] The samples annealed at 900°C, 950°C, and 1000°C for 12 h, seen in Figure 1, showed an increased phase fraction of the pyrochlore impurity with increasing temperature. Simply using the wolframite precursor and lowering the annealing temperature to 650°C resulted in samples with no pyrochlore impurity. Very small impurities (<1%) from remaining Bi and Na or K precursors could be seen after two 12 h annealing steps. These impurities were removed with 1 M nitric acid. To ensure that acid washing would not cause damage to the perovskite phase, degradation of the structure from exposure to concentrated nitric acid was investigated. Phase pure samples were exposed to concentrated nitric acid as described in the experimental section and XRD shows virtually no difference in relative intensities or peak broadening (see Figure S.1).

Attempts were made to sinter pellets into dense ceramics for properties measurements. Unfortunately, these materials could not be sintered using traditional methods. Raising the temperature above 650 °C for any duration resulted in formation of the pyrochlore phase. Previous studies of the piezoelectric properties on a similar system, (1-x)KNN-(x)$BiScO_3$ with x = 0.0-0.025, have used CuO sintering aids, indicating a difficulty in sintering even at low $BiScO_3$ concentrations.[34,35] Our attempts to add CuO did not result in dense pellets due to the much lower temperatures needed to maintain phase purity.

Synchrotron XRD data can be seen in Figure 2a and NPD data can be seen in Figure 2b. An impurity of < 1% $ScNbO_4$ that could not be observed during initial phase identification was identified. Visual inspection of the data indicates that $A = K^+$ has a cubic-like perovskite structure with no apparent peak splitting. However, peak splitting of the $(200)_c$ and $(310)_c$ peaks in XRD data is found for $A = Na^+$. The NPD data better illustrates the obvious difference between these materials. $A = K^+$ still shows a cubic-like perovskite structure, consistent with XRD data, but additional reflections are observed for $A = Na^+$. These reflections are pronounced in NPD, but only two of these peaks are observed in the XRD data (~10.4° and ~12.4°). The difference between XRD and NPD data indicates that these peaks are likely due to rotations of BO_6 octahedra because NPD is more sensitive to light elements such as oxygen. The presence of octahedral rotations in the Na^+ sample is easily explained by the Goldschmidt tolerance factor (t)

$$t = \frac{R_A + R_O}{\sqrt{2}\,(R_B + R_O)}$$

where R_O is the ionic radius of oxygen, and R_A and R_B are the ionic radii for the A-site and B-site cations respectively.[36] The tolerance factor is a simple calculation to determine the size ratio of the A-site to B-site cations. A material with t = 1 is likely to have a cubic structure and t < 1 is likely to exhibit octahedral rotations to increase electron orbital overlap and optimize the coordination environment between oxygen anions and the small A-site cations. Using ionic radii from Shannon yields t = 0.938 and 0.980 for $A = Na^+$ and K^+ respectively.[37] $A = K^+$ has a t close to 1 and logically crystallizes in a cubic-like structure. $A = Na^+$ has a t much smaller than 1, which indicates octahedral rotations will be present in the crystal structure.

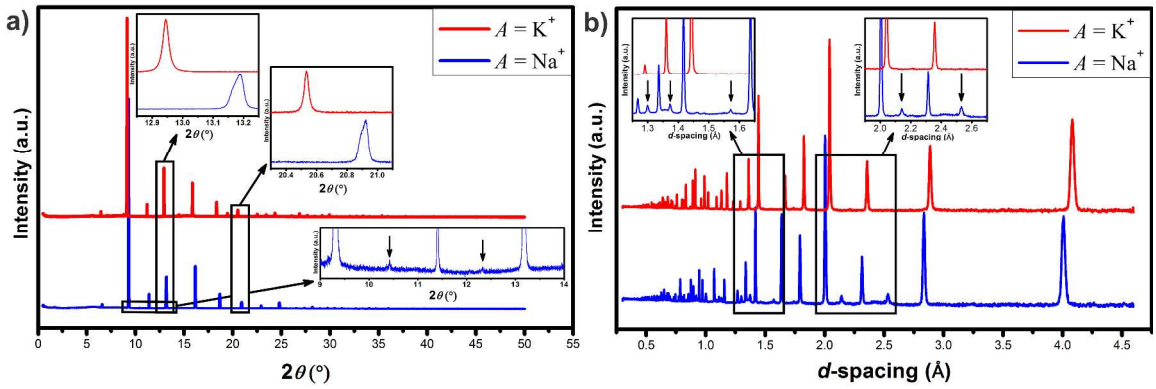

Figure 2. a) Synchrotron XRD data of $A = Na^+$ and K^+. Insets show peak splitting of $(200)_c$ and $(310)_c$ peaks present for $A = Na^+$ but not $A = K^+$ and octahedral rotation peaks at ~10.4° and ~12.4° for $A = Na^+$. **b)** NPD data for $A = Na^+$ and K^+. Insets show the emergence of octahedral rotation peaks for $A = Na^+$ but not $A = K^+$.

$Bi_{0.5}K_{0.5}Sc_{0.5}Nb_{0.5}O_3$

Ivanov *et al.* described $A = K^+$ as a distorted cubic structure by inspection of XRD data.[21] They mention that $BiScO_3$ favors rhombohedral distortions and that $Bi_{0.5}K_{0.5}Sc_{0.5}Nb_{0.5}O_3$ crystallizes in the $R\bar{3}m$ space group, which is nonpolar.[38] Their dielectric measurements showed a temperature of maximum permittivity, T_m, at ~427 °C, which they described as a relaxor transition (despite not showing a range of frequency data), which is inconsistent with centrosymmetric structures such as $R\bar{3}m$ and $Pm\bar{3}m$. In addition, their dielectric measurements were performed on samples with a large pyrochlore impurity of Bi_2ScNbO_7, which has relaxor properties at low temperatures.[31,32] Though the T_m of this pyrochlore is approximately -19 °C, the dielectric data from the literature is not entirely representative of the pure perovskite phase.

As an initial probe into the structure of the material, we performed SHG measurements on the phase pure samples. The SHG response was measured at 70 times that of α-SiO2, (Figure S.2). These results indicate that this material is non-centrosymmetric. Despite the SHG results, the synchrotron XRD data was best indexed to the cubic space group $Pm\bar{3}m$. In addition to investigating cubic symmetry, polar subgroups of $Pm\bar{3}m$ were considered to determine if a non-centrosymmetric structural model could be identified. *P*4*mm*, *Amm*2, and *R*3*m* are subgroups of $Pm\bar{3}m$ and are polar due to displacements in the (001), (110), and (111) directions, respectively. These space groups are consistent with $KNbO_3$, which transitions from *R*3*m* → *Amm*2 (room temperature phase) → *P*4*mm* → $Pm\bar{3}m$ from low to high temperature, similar to the phase transition sequence seen in $BaTiO_3$.[15,39]

Pawley fits were performed using the lattice parameters obtained from indexing XRD data. Refined lattice and profile parameters from the Pawley fits were used in the Rietveld refinements. Each space group symmetry tested accounted for all reflections in both XRD and NPD data. Each model fit the data well and fit quality parameters (R_{wp}) were 7.44 ($Pm\bar{3}m$), 6.90 (*P*4*mm*), 6.86 (*Amm*2), and 7.00% (*R*3*m*). Though visually and statistically these models fit well, all refinements resulted in large isotropic displacement parameters (B_{eq}) for the *A*-site cations (K^+ and Bi^{3+}) of 10.51 ($Pm\bar{3}m$), 10.73 (*P*4*mm*), 10.70 (*Amm*2), and 10.81 Å^2 (*R*3*m*). Relaxor materials typically have large *A*-site displacement parameters due to static disorder, which results in their observed properties For example lead in PSN has a B_{eq} of 4.33 Å^2 and the bismuth/barium site in $0.75Bi(Fe_{2/8}Ti_{3/8}Mg_{3/8})O_3$-$0.25BaTiO_3$ (BFTM-BT) has a B_{eq} of 7.3 Å^2.[40,41] However, the bismuth/potassium B_{eq} of 10 Å^2 in $Bi_{0.5}K_{0.5}Sc_{0.5}Nb_{0.5}O_3$ is anomalously large. In an attempt to account for this large B_{eq}, the atomic positions for K^+ and Bi^{3+} were unconstrained from each other for refinements with *P*4*mm*, *Amm*2, and *R*3*m* symmetry. An unconstrained *A*-site makes chemical sense because Bi^{3+} is known to stereochemically displace due to the inert pair effect, while K^+ prefers a more symmetric coordination environment.[39] Unconstraining the *A*-sites slightly dropped the R_{wp}, but the large *A*-site B_{eq} of 10.73 (*P*4*mm*), 10.70 (*Amm*2), and 10.70 Å^2 (*R*3*m*) is still observed. These improvements do not visually improve the fit of the data nor is there a reduction in the *A*-site displacement parameters. The largest improvement is observed in *R*3*m* fits which showed a 0.05% decrease in R_{wp} and a 0.11 Å^2 reduction in B_{eq}. Table S.1 summarizes the R_{wp}, χ^2, and *A*-site B_{eq} for the $Pm\bar{3}m$ fit and *P*4*mm*, *Amm*2, and *R*3*m* fits that have unconstrained *A*-sites and the final Rietveld refinements of these data can be seen in Figure S.3.

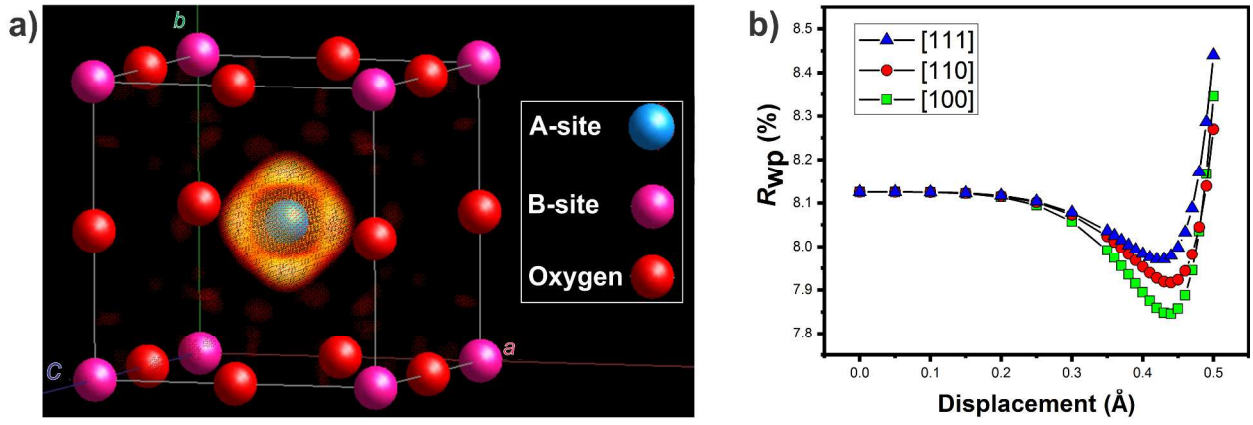

Figure 3. a) Fourier difference map for $A = K^+$ which was calculated from the Rietveld refinement in $Pm\bar{3}m$ on XRD data. **b)** Displacement analysis results showing the R_{wp} as a function *A*-site cation displacement in the [100], [110] and [111] directions.

The Fourier difference map calculated from $Pm\bar{3}m$ fits to XRD data can be seen in Figure 3a. Electron density is missing from the area surrounding the *A*-site, consistent with the large isotropic displacement parameter. The missing electron density is distributed anisotropically and is projecting towards the faces of the unit cell. PSN[40,42], $BaTiO_3$[43], $Pb(Mg_{1/3}Nb_{2/3})O_3$ (PMN)[44], and BFTM-BT[41] also have large atomic displacement parameters on their *A*-sites, commonly due to static disorder from cation substitution. Therefore, the next step in the refinement was to investigate a distorted cubic model to account for the large displacement parameters and a cubic-like structure with local distortions.[40–44] This distorted cubic model has the same lattice parameters, *B*-site position (1a), and *O*-site position (3d) that are used in the $Pm\bar{3}m$ space group, but the *A*-site cation is moved off of its special position. The model is considered distorted because the *A*-site cation is displaced from its crystallographic position usually found at the center of the AO_{12} polyhedra (1b). Refinements were performed allowing the displacement parameters to refine. However, the *A*-site cation was not allowed to refine, but it's position was manually and systematically moved in various crystallographic directions while monitoring the R_{wp}. These results can be seen in Figure 3b for displacements in the [100], [110] and [111] directions.

There is a clear minimum in the R_{wp} for all three displacement directions at 0.44 Å, with [100] showing the deepest minima. This *A*-site displacement distance is larger than that seen in most other materials. The minimum in the displacement for PSN is at 0.33 Å in the [111] direction, for $BaTiO_3$ it is at 0.11 Å in the [110] direction, for PMN it is at ~0.22 Å in the [100] direction or ~0.31 Å in the [110] and [111] directions, and for BFTM-BT it is ~0.5 Å but the three directions are indistinguishable from each other.[40–44] The only material with a larger displacement distance is BFTM-BT.

The $A = K^+$ model with a displacement of 0.44 Å along [100] was further refined allowing the atomic position to freely move and yielded a final displacement distance of 0.435 Å along [100]. This fit yielded an R_{wp} of 7.05% and a more reasonable *A*-site B_{eq} of 4.59 $Å^2$. Though the R_{wp} is not the lowest of all of the space groups investigated, the combination of a low R_{wp}, a good visual fit to the data, and the most reasonable *A*-site B_{eq} makes the [100] distorted cubic model the best description of the average structure for these data. Though a centrosymmetric space group precludes SHG activity, cubic relaxors, such as PMN, have shown SHG activity due to local scale symmetry breaking.[45] Final Rietveld refinements of the XRD and NPD data for the [100] distorted cubic model can be seen in Figure 4 and the refined values can be seen in Table 1.

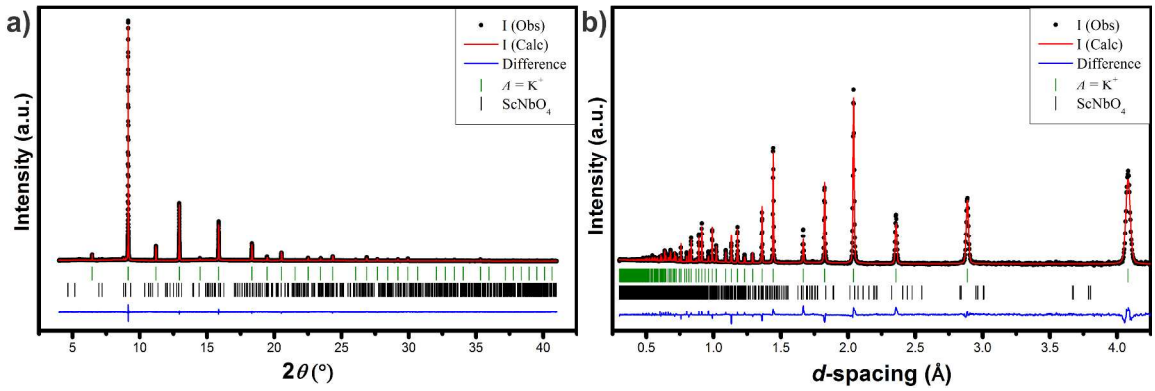

Figure 4. Results of combined Rietveld refinement of $A = K^+$ in $Pm\bar{3}m$ with [100] distortion using **a)** synchrotron XRD and **b)** NPD data. Black circles are observed data, red lines are calculated Rietveld models, blue lines are the difference between observed and calculated patterns, and green markers indicated *hkl* positions for the space group.

Table 1. Refined atomic positions, occupancies, isotropic displacement parameters, and lattice parameters for $A = K^+$.

$Pm\bar{3}m$		R_{wp} = 7.05 %		χ^2 = 2.82		
Atom	**Site**	**X**	**Y**	**Z**	**Occ**	**B_{eq}**
Bi	6f	0.6066(3)	0.5	0.5	1/12	4.59(6)
K	6f	0.6066(3)	0.5	0.5	1/12	4.59(6)
Sc	1a	0	0	0	1/2	0.905(5)
Nb	1a	0	0	0	1/2	0.905(5)
O	3d	0	0	0.5	1	2.286(8)
a = 4.081343(4) Å						

Our original synthetic procedure for $Bi_{0.5}K_{0.5}Sc_{0.5}Nb_{0.5}O_3$ resulted in a highly symmetric unit cell with significant disorder of the *A*-site cation. We also investigated this composition using a different synthetic route to manipulate the degree of *B*-site ordering in the system. A difference in oxidation state of two or greater, such as in Sc^{3+} and Nb^{5+}, has been shown to lead to rock salt ordering of *B*-site cations[2,33] so to examine the possibility of ordering, the sample was subjected to long annealing times. Rock salt ordering of *B*-site cations in an ideal cubic perovskite doubles the lattice parameters and transforms symmetry from $Pm\bar{3}m$ to $Fm\bar{3}m$, which is identified by the emergence of a supercell reflection at low

2θ in XRD patterns.[1,33] For Sc^{3+} and Nb^{5+} this transformation is not always complete, as is the case for $NaLaScNbO_6$, which shows 84% cation ordering by Rietveld analysis or PSN, which shows between 18 and 91% ordering, depending on the annealing time.[2,33] PSN has polar rhombohedral distortions, and the degree of ordering has a significant impact on the relaxor and ferroelectric properties, allowing for precise synthetic control of these properties. It has been shown that ordering of Sc^{3+} and Nb^{5+} changes the nature of the samples from relaxor ferroelectric to normal ferroelectric as seen by a reduction in T_m, a reduction in the frequency dispersion of T_m (ΔT_m), and the temperature dependence of polarization versus electric field loops.[33]

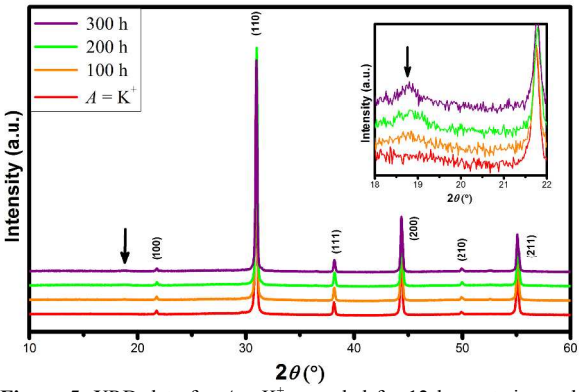

Figure 5. XRD data for $A = K^+$ annealed for 12 hours twice and samples subsequently annealed for 100 h, 200 h, and 300 h. Inset shows the emergence of a peak at 18.8°, consistent with a doubling of the lattice parameter.

Figure 5 shows the XRD patterns for $A = K^+$ samples as prepared and annealed for 100 h, 200 h, and 300 h after phase formation. The emergence of a broad peak at 2θ = 18.8° is observed, consistent with the predicted position for the doubling of the primitive cubic unit cell. When analyzing the relationship between annealing time and *B*-site ordering in PSN Zhu *et al.* used the ratio of integrated intensity of diffraction peaks

$$S = \sqrt{\frac{\left(\frac{I_o}{I_{100}}\right)_{Expt}}{\left(\frac{I_o}{I_{100}}\right)_{Calc}}}$$

where S is the degree of *B*-site ordering, I_o is the integrated intensity of the superlattice reflection, I_{100} is the integrated intensity of the $(100)_c$ peak, and Expt and Calc refer to experimental and calculated intensities respectively.[33] The S values calculated for PSN were 0.18, 0.61, and 0.91 for samples as prepared (1300 °C, 2h) and subsequently annealed at 1000 °C for 25 h and 50 h, respectively. For $A = K^+$, S was determined to be 0, 0.22, 0.38, and 0.44 for the as prepared (650 °C, 24h), 100h, 200h, and 300h samples respectively. Whether *B*-site ordering in Bi(*A*)$ScNbO_6$ compounds is less thermodynamically favorable or kinetically inhibited by the low annealing temperature is not clear and should be investigated further

$Bi_{0.5}Na_{0.5}Sc_{0.5}Nb_{0.5}O_3$

The only report of the $A = Na^+$ composition in the literature is by Knapp in her thesis from 2006.[20] Knapp fit lab XRD data using the Pawley method and reported the material to have the space group *Pnma*. Significant pyrochlore impurities can be seen similar to previously published reports on $A = K^+$. The *Pnma* space group is a reasonable model as previous structural studies on one of the parent compound, $NaNbO_3$, indicate it has the same symmetry.[14,46] However, our high resolution synchrotron XRD data was initially indexed to *P*4/*mbm* symmetry, consistent with another high temperature phase of $NaNbO_3$.[14,47] Due to the inconstancies between indexing and previous results, as well as the complex structure that $NaNbO_3$ exhibits, combined Rietveld refinements of NPD and synchrotron XRD were performed using *P*4/*mbm*, *Cmcm*, *Pbnm*, *Pbcm*, *R*3*c*, and $P2_1/m$ symmetries, as those are the previously reported space groups for $NaNbO_3$ at low, ambient, and high temperatures.[14,48] Rietveld refinements for all space groups investigated can be seen in Figure S.4 and Table 2 summarizes lattice parameters, tilt systems, R_{wp}, χ^2, *A*-site isotropic displacement parameters, and the number of *hkl*s in the model that have no corresponding peak in the data for all refinements.

Table 2. Space group, lattice setting, glazer tilt system, fit quality parameters, *A*-site isotropic displacement parameters, and number of *hkl*s in the model with no corresponding peak in the data from 6.5 to 2.0 Å.

Crystal System	Space Group	Lattice Parameters			Tilts	R_{wp}	χ^2	B_{eq}†	*hkl*s‡
		a	*b*	*c*					
Tetragonal	*P*4/*mbm*	$\sqrt{2}a$	$\sqrt{2}a$	*a*	$a^+a^+a^+$	9.22	3.57	6.41(2)	0
Orthorhombic	*Cmcm*	2*a*	2*a*	2*a*	$a^+b^-c^-$	7.94	2.65	6.51(2)	8
Orthorhombic	*Pbnm*	$\sqrt{2}a$	$\sqrt{2}a$	2*a*	$a^-a^-c^+$	8.11	2.77	6.49(2)	7
Orthorhombic	*Pbcm*	$\sqrt{2}a$	$\sqrt{2}a$	4*a*	$a^-a^-c^+$	8.24	2.85	6.44(2)	23
Rhombohedral	*R*3*c*	2*a*	2*a*	2*a*	$a^-a^-a^-$	8.47	3.02	6.63(2)	5
Monoclinic	$P2_1/m$	$\sqrt{2}a$	2*a*	$\sqrt{2}a$	$a^+b^-c^-$	7.97	2.67	6.36(2)	13

† isotropic displacement parameter of the *A*-site Cation
‡ number of reflections in the model with no corresponding reflection in the experimental data from 6.5 to 2.0 Å

Each space group investigated accounts for all observed reflections seen in NPD and XRD data sets, but the lower symmetry space groups have many additional reflections in the models that are not observed in the experimental data. A large B_{eq} for *A*-site cations, from 6.36 to 6.64 $Å^2$, is observed regardless of the space group investigated. Visually, all appear to model the data well. The fits of select XRD peaks can be seen in Figure S.5. Inspection of the models eliminated $P2_1/m$ and *R*3*c* as options despite their low R_{wp}. Both of these monoclinic and rhombohedral symmetries poorly fit the splitting of the $(200)_c$ reflection and they showed the largest intensity mismatch for the $(110)_c$ reflection. The $(100)_c$ reflection was poorly fit by $P2_1/m$ and the *R*3*c* fit and there was a significant intensity mismatch with the $(111)_c$ reflection. In addition, NPD fits using these two symmetries showed many reflections in the fits that are not observed in the data. The orthorhombic and tetragonal space groups all fit the XRD data well. However, they all consistently show the large mismatches with the $(100)_c$ reflection and the $(111)_c$ reflection. The fits for the $(100)_c$ reflection show a small position mismatch with the model having a larger 2θ

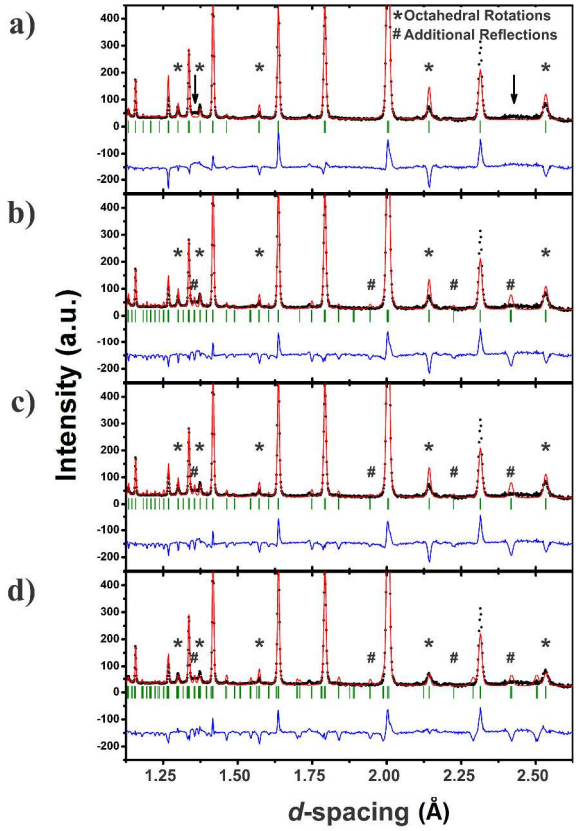

Figure 6. Rietveld refinements of A = Na^+ NPD data from d = 1.175 to 2.626 Å for **a)** *P4/mbm*, **b)** *Cmcm*, **c)** *Pbnm*, and **d)** *Pbcm* symmetries. Reflections associated with octahedral rotations are marked with *, additional reflections in the models that do not show a corresponding reflection in the data are marked with #, and arrows highlight areas that show diffuse scattering. Black circles are observed data, red lines are calculated Rietveld models, blue lines are the difference between observed and calculated patterns, and green markers indicated *hkl* positions for the space group.

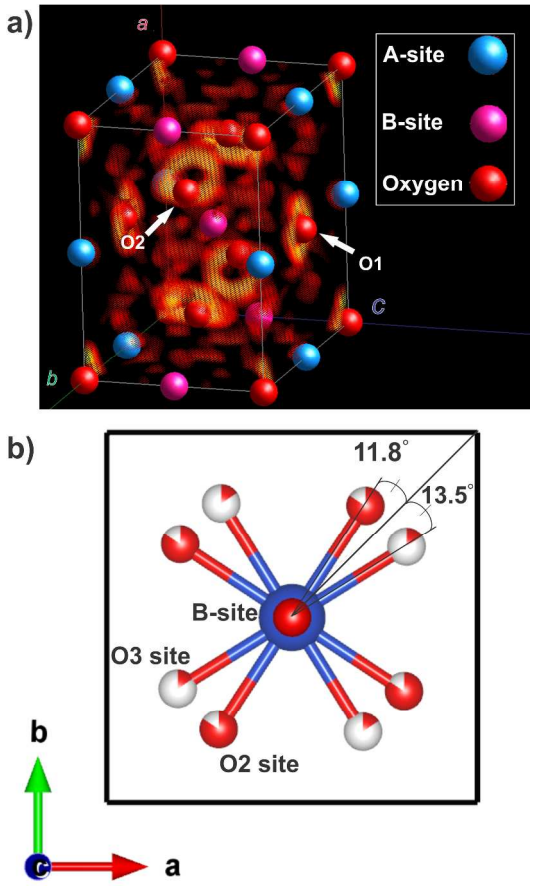

Figure 7. **a)** Fourier difference map calculated for A = Na^+ from the Rietveld refinement in *P4/mbm* on NPD data. **b)** Schematic of a BO_6 octahedra in a *P4/mbm* unit cell, looking down the *c*-axis. Blue spheres represent *B*-sites, red spheres are oxygens, and white indicates a fractional occupancy. Schematic shows both the anticlockwise rotation of the O2 position and the clockwise rotation of the O3 position.

position. The $(111)_c$ reflection shows predominantly an intensity mismatch with *Cmcm* fitting the best and *Pbcm* fitting very poorly both in intensity and position.

A comparison of the NPD fits from d = 1.175 – 2.625 Å for the orthorhombic and tetragonal space groups can be seen in Figure 6. The selected range highlights reflections at 1.30, 1.37, 1.57, 2.14, and 2.53 Å, which are associated with octahedral rotations. All of the symmetries investigated account for these octahedral rotation peaks, but the orthorhombic space groups have many additional reflections in the model that are not observed in the data. All orthorhombic space groups have additional peaks in the model at d = 1.36, 1.94, 2.22, and 2.41 Å. Many other additional peaks and *hkl* positions can be seen that are specific to each space group. Only the *P4/mbm* space group can account for all peaks without additional and unnecessary *hkl*s, leading us to believe this material has tetragonal symmetry. *P4/mbm* is a centrosymmetric structure, which is also consistent with the lack of SHG activity that we measured for A = Na^+.

At d ~1.35 Å and ~2.41 Å there is observed scattering intensity in the NPD data found above the calculated background function, as indicated by arrows in Figure 6a. This scattering intensity does not appear to be from low intensity Bragg reflections but from local diffuse scattering. Looking at fits with orthorhombic symmetry (Figure 6b-d), there are sharp Bragg peaks associated with antiphase tilting of the BO_6 octahedra in these regions. Antiphase tilting is seen in every other space group we investigated, other than *P4/mbm*. The Fourier difference map of the NPD data using the tetragonal fit can be seen in Figure 7a. An annulus of missing scattering intensity is found around the O2 oxygen position on one side. The annulus is centered where the oxygen would be if there were no rotations of the octahedra, indicating out of phase tilting could be present. Fits performed using *I4/mcm* symmetry were therefore investigated because the $a^oa^oa^-$ rotation pattern has antiphase tilting along the *c*-axis, the same direction as the in-phase tilts of *P4/mbm*. The refinements showed that the *I4/mcm* symmetry does not account for many of the reflections seen in the NPD data.

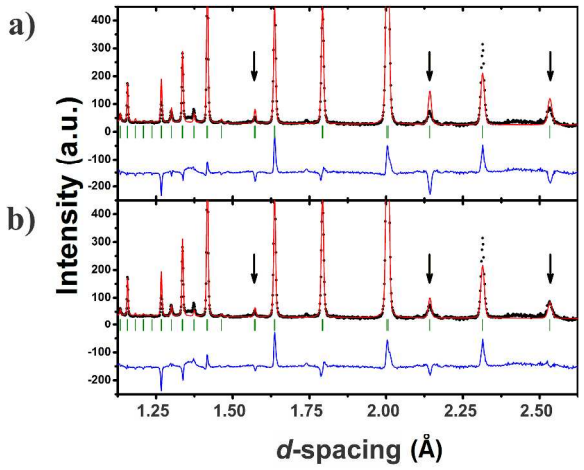

Figure 8. Rietveld refinements of A = Na^+ on NPD data from 1.175 to 2.626 Å for *P*4/*mbm* with **a)** its standard $a^0a^0a^+$ tilting scheme and **b)** disordered tilting from a split equatorial oxygen site. Black circles are observed data, red lines are calculated Rietveld models, blue lines are the difference between observed and calculated patterns, and green markers indicated *hkl* positions for the space group.

To account for the missing scattering intensity, the equatorial oxygen (O2) was spilt into two sites, see Figure 7b. The new equatorial oxygen (O3) position was set to have the same rotation direction (along the *c*-axis) and angle as O2 (10.6°), but to have a clockwise rotation instead of anticlockwise. The occupancy of these sites was set equal to each other and constrained to equal the proposed stoichiometry. The atomic positions and then the occupancy were refined iteratively and then together. This fit resulted in a rotation angle for O3 that is slightly larger than the O2 rotation angle, 13.5° clockwise and 11.8° anticlockwise, and a 15% occupancy of the O3 site. Both rotations are larger in magnitude than the original *P*4/*mbm* fit, which had a 10.6° anticlockwise rotation. Fits of the NPD data from d = 1.175 – 2.625 Å both with and without the split oxygen site can be seen in Figure 8a and b respectively. The split oxygen site significantly decreases the intensity mismatch of octahedral rotation peaks, specifically at d = 1.57, 2.14, and 2.53 Å. The tilt disorder also reduces the R_{wp} from 9.22 to 8.88% and slightly decreases the B_{eq} from 6.41 to 6.36 $Å^2$. Multiphase refinements of *P*4/*mbm* and *I*4/*mcm* were considered, but the peak broadening seen in XRD and NPD is fit satisfactorily with one phase data does not support the existence of two phases. Local scale twining of may also be an appropriate model, but we see no indication of supercell reflections that would justify a larger unit cell.

The Fourier difference map of the NPD data, fit in *P*4/*mbm*, with the split oxygen site can be seen in Figure S.6. The Fourier difference map shows that splitting the oxygen position does not account for all the missing scattering intensity. This mismatch between the model and the data means that the local tilt disorder is not sufficiently described by an out of phase tilting pattern because it is contingent on the local environment of the adjacent unit cells. We suspect that the local tilting disorder is more complicated than what can be described by a model of the average structure. Each individual unit cell has a tolerance factor range from 0.967 ($NaNbO_3$) to 0.910 ($BiScO_3$). With this wide range of local chemical environments, it is possible that the diffuse scattering seen in NPD data is due to local, chemically ordered regions that are highly strained nanodomains. Each domain could have different tilting schemes as described by orthorhombic or monoclinic symmetry. Local orthorhombic distortions have been observed in other $NaNbO_3$ based materials, but our analysis cannot clearly identify any because they are not manifested in a long range order.[46,49]

After careful examination of all the models, we have concluded that due to the improved intensity matching of tilting reflections and the improvement in fit quality parameters when splitting the oxygen site, that this material is best described by *P*4/*mbm* symmetry with disordered rotation of the BO_6 octahedra. Further studies to determine the local structure are necessary to understand the disorder at the local scale. The final Rietveld refinements of the XRD and NPD data can be seen in Figure 9 and a table of refined values can be seen in Table 3.

Table 3. Refined atomic positions, occupancies, isotropic displacement parameters, and lattice parameters for A = Na^+.

P4/mbm		R_{wp} = 8.88 %		χ^2 = 3.32		
Atom	**Site**	**X**	**Y**	**Z**	**Occ**	**B_{eq}**
Bi	2d	0.5	0	0	0.5	6.36(2)
Na	2d	0.5	0	0	0.5	6.36(2)
Sc	2b	0	0	0.5	0.5	1.034(8)
Nb	2b	0	0	0.5	0.5	1.034(8)
O1	2a	0	0	0	1	3.36(3)
O2	4h	0.6977	0.1977(4)	0.5	0.850(3)	3.36(3)
O3	4h	0.810	0.310(2)	0.5	0.150	3.36(3)
a = 5.66489(2) Å			c = 4.01260(2) Å			

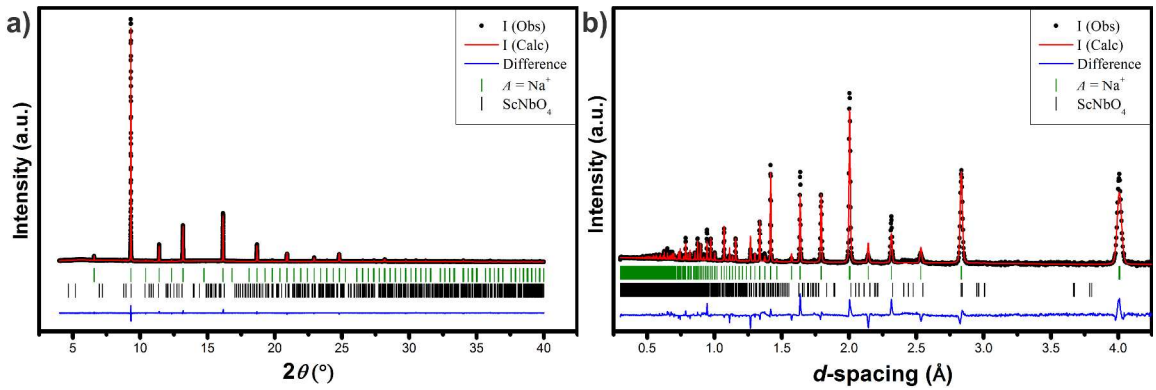

Figure 9. Results of the combined Rietveld refinement of $A = Na^+$ in *P4/mbm* with distorted tilting using **a)** synchrotron XRD and **b)** NPD data. Black circles are observed data, red lines are calculated Rietveld models, blue lines are the difference between observed and calculated patterns, and green markers indicated *hkl* positions for the space group.

Discussion

The final refined structure of both $A = K^+$ and Na^+ can be seen in Figure 10a and b respectively. Both compounds show similar phase behavior to each other and to other $BiScO_3$ solid solutions. Both compounds have structures that are high temperature phases of their $(A)NbO_3$ parent compound. $KNbO_3$ is *Amm*2 at room temperature and transitions to *P*4*mm* and $Pm\bar{3}m$ at high temperature.[39] $NaNbO_3$ transitions from *Pbcm* at room temperature to *Pbnm*, then *Cmcm*, then *P*4/*mbm*, and finally $Pm\bar{3}m$ when heating.[14] Though $A = Na^+$ has not gone fully cubic, like $A = K^+$ did, its room temperature structure is isostructural with one of the high temperature phases of $NaNbO_3$. This increase in symmetry is common for solid solutions of perovskites with $BiScO_3$.

$BaTiO_3$ and KNN both increase in symmetry when substituting $BiScO_3$ into the lattice, changing from *P*4*mm* to $Pm\bar{3}m$ and from *Amm*2 to *P*4*mm* to $Pm\bar{3}m$ respectively.[50,51] This structural transition results from the addition of bismuth, which is prone to a lone pair distortion, to an end member where the *A*-site prefers a more symmetrical environment. This addition of bismuth changes the symmetry via chemical pressure rather than temperature, where the strain between the preferred coordination environments of the two *A*-site cations results in relaxor ferroelectric behavior. Alternatively, $PbTiO_3$-$BiScO_3$ solid solutions decrease in symmetry and favor rhombohedral distortions with increasing $BiScO_3$ concentration, changing from *P*4*mm* to *R*3*m* to *R*3*c*.[38] When two atoms with a lone pair distortion are found at the *A*-site such as in this solid solution, a non-centrosymmetric structure along with classical ferroelectric and piezoelectric properties are maintained over a larger composition range.[38,52] The $A = Na^+$ and K^+ materials are essentially $(1-x)(A)NbO_3$-$xBiScO_3$ solid solutions, where $x = 0.5$. From this perspective it makes sense that $A = Na^+$ and K^+ would behave more like KNN and $BaTiO_3$ than $PbTiO_3$ because one end member of the solid solution does not have a lone pair cation on the *A*-site. It is possible that these $(A)NbO_3$-$BiScO_3$ solid solutions could transition through all of the high temperature phases of the $(A)NbO_3$ end member, should the entire composition range be synthesized and characterized.

In particular, we find $(Bi_{0.5}K_{0.5})(Sc_{0.5}Nb_{0.5})O_3$ to be very interesting. When examining the end members of this solid solution, $KNbO_3$ has a polar [110] displacement and $BiScO_3$ favors [111] displacements.[38,39] The equal molar combination of these two phases has increased the symmetry from the end members. Solid solutions where $0 < x < 0.5$ should be investigated further. We believe that as the amount of $BiScO_3$ increases, there could be a phase transition sequence similar to that found in the temperature dependent $KNbO_3$ phase transitions where the displacement direction changes from [110] in the *Amm*2 space group to [001] in the *P*4*mm* space group before transforming to the distorted cubic structure observed in the $x = 0.5$ composition. This sequence opens up the possibility of finding a morphotropic phase boundary (MPB) in $KNbO_3$-$BiScO_3$ solid solutions where an enhanced piezoelectric response would be found. This MPB would occur at the boundary between the *Amm*2 and *P*4*mm* structures.

KNN-$BiScO_3$, is also believed to transition from [110] to [001] polarization before becoming cubic, but the crystallography is still unknown.[51] A recent crystallographic study of the pair distribution function of $BaTiO_3$-$BiScO_3$ that created large-box models to fit both the average and local structural data showed a similar result to our Rietveld model. Their Rietveld analysis was performed on compositions of the cubic side of the transition and also shows large isotropic displacement parameters.[53] The results of their large-box modeling found that a distorted cubic structure with both [100] and [111] displacements best described the structure.

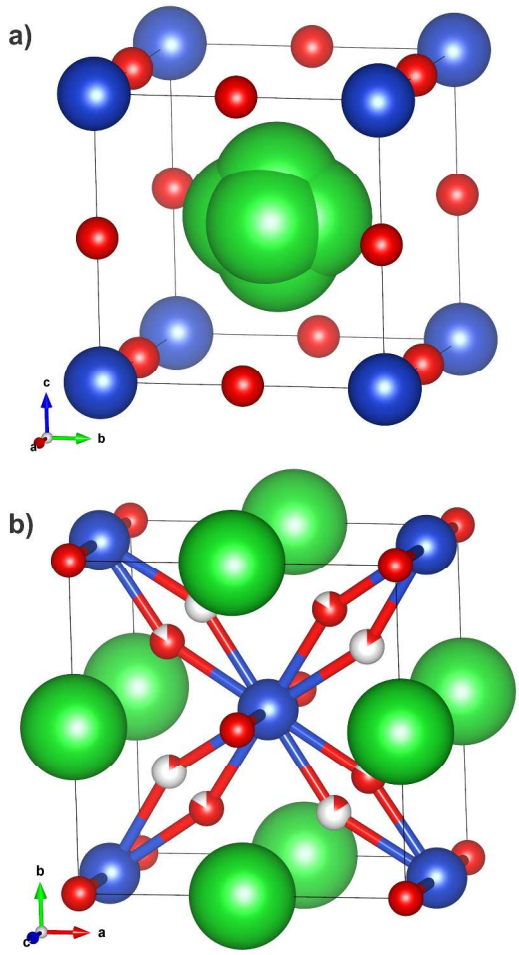

Figure 10. Schematic of the structures resulting from the combined Rietveld refinement on **a)** $A = K^+$ in $Pm\bar{3}m$ with [100] distortions and **b)** $A = Na^+$ in *P4/mbm* with disordered tilts. Green spheres represent *A*-sites, blue spheres represent *B*-sites, red spheres are oxygens, and white indicates a fractional occupancy.

The structure of end member $NaNbO_3$ has been shown to be particularly sensitive to temperature, substitution, and synthetic method.[14,46,54–56] Variable temperature neutron studies show that there is phase coexistence between *R*3*c* and *Pbcm* below room temperature and between *Pbnm* and *Cmcm* above room temperature.[14] Sol-gel and nanoparticle synthesis have been shown to modify the room temperature structure from non-polar *Pbcm* to polar $Pma2_1$ and $Pmc2_1$ respectively.[46,55] Additionally, small quantities of substitution can cause phase changes. As little as 5% Li substitution onto the *A*-site shows a phase transformation to the polar space group $Pma2_1$.[56] Whether the structural differences between the naturally occurring $NaNbO_3$ mineral, leushite, and synthetically derived $NaNbO_3$ are from minuscule impurities or different synthetic conditions is not clear, but it reaffirms that the structure of $NaNbO_3$ is highly sensitive.[54]

Phase coexistence may help explain the diffuse scattering seen in NPD data for $A = Na^+$. Small nanodomains with different tilt patterns may exist, but are not detectable by Bragg diffraction. Local structural investigations of these new compositions are strongly encouraged as they may lead to the discovery of the existence of new and interesting phases. Further investigation on the synthetic control of structural and physical properties of $A = Na^+$ and K^+ should also be performed as they may be viable options for new, lead-free relaxor materials.

It is very clear that the structure of these $(Bi_{0.5}A_{0.5})(Sc_{0.5}Nb_{0.5})O_3$ materials are highly sensitive to synthetic conditions just like the parent $NaNbO_3$. Subjecting the solid solutions or its precursors to temperatures above 650 °C for any duration of time causes formation of a pyrochlore impurity. These impurities prevented the densification of pellets by standard synthesis methods. However, it is possible that dense pellets may be formed by hot pressing[57], spark plasma sintering[58], or cold sintering[59], and should be investigated in the future to determine the properties of the entire solid solution.

The preparation of these materials is not only sensitive to temperature, but also to time, as evidenced by the ordering of *B*-site cations in $A = K^+$. The physical properties of PSN have been shown to be highly dependent on *B*-site ordering.[23] The relaxor properties of $A = K^+$ would presumably behave similarly. Due to the same *B*-site composition as $A = K^+$ and PSN it is likely that the *B*-sites would order if heated for long enough, but, due to differences in ionic radii, it is more likely that long range ordering of the *A*-sites would emerge. *A*-site ordering rarely occurs without *B*-site ordering and even if *B*-sites are ordered, *A*-site ordering is sensitive to cation size differences.[1] Knapp showed simultaneous *B*-site and *A*-site ordering occurs in $LaNaScNbO_6$, and the ionic radii of Bi^{3+} and La^{3+} are similar when in the 12-fold coordination of the *A*-site in a perovskite. The requirements for *A*-site and *B*-site ordering are present, which may lead to similar ordering behavior between $A = Na^+$ and $LaNaScNbO_6$.[2]

Conclusions

The perovskites $(Bi_{0.5}A_{0.5})(Sc_{0.5}Nb_{0.5})O_3$, where $A = K^+$ and Na^+, have been synthesized without pyrochlore impurities for the first time. A distorted cubic structure with *A*-site displacement in the [100] directions is seen for the average structure of $A = K^+$, and tetragonal *P*4/*mbm* symmetry with octahedral rotations along the *c*-axis best describes the average structure of $A = Na^+$. Regardless of having a centrosymmetric structure, $A = K^+$ is second harmonic generation active because of the local polar distortions, which is consistent with the previously measured relaxor properties. The structure is sensitive to synthetic procedure, showing *B*-site ordering after very long annealing times, similar to PSN. Both structures likely have significant disorder, which merits further study into their local distortions. Diffuse scattering is seen in the NPD data for $A = Na^+$, which may suggest that its structure is also sensitive to synthesis conditions. These materials may possess interesting relaxor or piezoelectric properties and their low temperature synthesis make them interesting targets for thin film synthesis.

Conflicts of interest

Authors declare that that is no conflicts of interest regarding this research.

Acknowledgements

Michelle Dolgos and Alicia Manjón-Sanz would like to thank the NSF (DMR-1606909) for support. T. Thao Tran would like to thank the NSF (DMR-1503573) for support. The authors would like to thank the Halasyamani Group at University of Houston for their SHG analysis and to Dr. Halasyamani for his useful discussion. Use of the Advanced Photon Source at Argonne National Laboratory was supported by the U.S. Department of Energy, Office of Science, Office of Basic Energy Sciences, under Contract No. DE-AC02-06CH11357. This research used resources at the Spallation Neutron Source, a DOE Office of Science User Facility operated by the Oak Ridge National Laboratory. We would like to thank Saul Lapidus and Lynn Ribaud of 11-BM at the APS and Ashfia Huq, Pam Whitfield, and Melanie Kirkham of POWGEN at the SNS for their assistance with our experiments.

References

(1) King, G.; Woodward, P. M. *J. Mater. Chem.* **2010**, *20* (28), 5785–5796.
(2) Knapp, M. C.; Woodward, P. M. *J. Solid State Chem.* **2006**, *179* (4), 1076–1085.
(3) Fabini, D. H.; Siaw, T. A.; Stoumpos, C. C.; Laurita, G.; Olds, D.; Page, K.; Hu, J. G.; Kanatzidis, M. G.; Han, S.; Seshadri, R. *J. Am. Chem. Soc.* **2017**, *139* (46), 16875–16884.
(4) Sleight, A. W. *Phys. C Supercond. its Appl.* **2015**, *514*, 152–165.
(5) Wadekar, P. V.; Alaria, J.; O'Sullivan, M.; Flack, N. L. O.; Manning, T. D.; Phillips, L. J.; Durose, K.; Lozano, O.; Lucas, S.; Claridge, J. B.; Rosseinsky, M. J. *Appl. Phys. Lett.* **2014**, *105* (5), 1–5.
(6) Malavasi, L.; Kim, H.; Proffen, T. *J. Appl. Phys.* **2009**, *105* (12), 123519.
(7) Subramanian, M. A.; Sleight, A. W. *Solid State Sci.* **2002**, *4* (3), 347–351.
(8) Dolgos, M. R.; Adem, U.; Manjón-Sanz, A.; Wan, X.; Comyn, T. P.; Stevenson, T.; Bennett, J.; Bell, A. J.; Tran, T. T.; Halasyamani, P. S.; Claridge, J. B.; Rosseinsky, M. J. *Angew. Chemie - Int. Ed.* **2012**, *51* (43), 10770–10775.
(9) McQuade, R. R.; Dolgos, M. R. *J. Solid State Chem.* **2016**, *242*, 140–147.
(10) Mandal, P.; Pitcher, M. J.; Alaria, J.; Niu, H.; Borisov, P.; Stamenov, P.; Claridge, J. B.; Rosseinsky, M. J. *Nature* **2015**, *525* (7569), 363–366.
(11) Aleksandrov, K. S.; Bartolomé, J. *Phase Transitions* **2001**, *74* (3), 255–335.
(12) Stokes, H. T.; Kisi, E. H.; Hatch, D. M.; Howard, C. J. *Acta Crystallogr. Sect. B* **2002**, No. B58, 934–938.
(13) Lefkowitz, I.; Łukaszewicz, K.; Megaw, H. D. *Acta Crystallogr.* **1966**, *20* (5), 670–683.
(14) Jiang, L.; Mitchell, D. C.; Dmowski, W.; Egami, T. *Phys. Rev. B* **2013**, *88* (1), 14105.
(15) Von Hippel, A. *Rev. Mod. Phys.* **1950**, *22* (3), 221–237.
(16) Senn, M. S.; Keen, D. A.; Lucas, T. C. A.; Hriljac, J. A.; Goodwin, A. L. *Phys. Rev. Lett.* **2016**, *207602* (May), 1–5.
(17) Zhang, N.; Yokota, H.; Glazer, A. M.; Ren, Z.; Keen, D. A.; Keeble, D. S.; Thomas, P. A.; Ye, Z. G. *Nat. Commun.* **2014**, *5* (May), 1–9.
(18) Jo, W.; Dittmer, R.; Acosta, M.; Zang, J.; Groh, C.; Sapper, E.; Wang, K. **2014**, No. 2012, 71–93.
(19) Bokov, A. A.; Ye, Z. G. *J. Mater. Sci.* **2006**, *41* (1), 31–52.
(20) Knapp, M. C. Thesis, Ohio State University, 2006.
(21) Ivanov, O.; Danshina, E.; Sudzhanskaya, I.; Vasil'ev, A. *Phys. status solidi - Rapid Res. Lett.* **2014**, *8* (2), 198–201.
(22) Swartz, S. L.; Shrout, T. R. *Mater. Res. Bull.* **1982**, *17* (10), 1245–1250.
(23) Zhu, M.; Chen, C.; Tang, J.; Hou, Y.; Wang, H.; Yan, H.; Zhang, W.; Chen, J.; Zhang, W. *J. Appl. Phys.* **2008**, *103* (8), 0–6.
(24) Wang, J.; Toby, B. H.; Lee, P. L.; Ribaud, L.; Antao, S. M.; Kurtz, C.; Ramanathan, M.; Von Dreele, R. B.; Beno, M. A. *Rev. Sci. Instrum.* **2008**, *79* (8), 0–7.
(25) Huq, a; Hodges, J. P.; Gourdon, O.; Heroux, L. *Zeitschrift für Krist. Proc.* **2011**, *1* (November 2011), 127–135.
(26) Coelho, A. *J. Appl. Crystallogr.* **2000**, *33* (3 Part 2), 899–908.
(27) Stephens, P. W. *J. Appl. Crystallogr.* **1999**, *32* (2), 281–289.
(28) Dianoux, A.-J.; Lander, G. *Neutron Data Booklet*; OCP Science: Phillidelphia, PA, 2003.
(29) Sears, V. F. *Neutron News* **1992**, *3* (3), 26–37.
(30) Ok, K. M.; Chi, E. O.; Halasyamani, P. S. *Chem. Soc. Rev.* **2006**, *35* (8), 710–717.
(31) Cann, D. P.; Randall, C. A.; Shrout, T. R. *Solid State Commun.* **1996**, *100* (7), 529–534.
(32) Liu, Y.; Withers, R. L.; Nguyen, H. B.; Elliott, K.; Ren, Q.; Chen, Z. *J. Solid State Chem.* **2009**, *182* (10), 2748–2755.
(33) Zhu, M.; Chen, C.; Tang, J.; Hou, Y.; Wang, H.; Yan, H.; Zhang, W.; Chen, J.; Zhang, W. *J. Appl. Phys.* **2008**, *103* (8), 84124.
(34) Li, X.; Jiang, M.; Liu, J.; Zhu, J.; Zhu, X.; Li, L.; Zhou, Y.; Zhu, J.; Xiao, D. *Phys. Status Solidi* **2009**, *206* (11), 2622–2626.
(35) Liu, J.; Zhu, J.; Li, X.; Wang, M.; Zhu, X.; Zhu, J.; Xiao, D. *Mater. Lett.* **2011**, *65* (6), 948–950.
(36) Goldschmidt, V. M. *Naturwissenschaften* **1926**, *14* (21), 477–485.
(37) Shannon, R. D. *Acta Crystallogr. Sect. A* **1976**, *32* (5), 751–767.
(38) Eitel, R. E.; Zhang, S. J.; Shrout, T. R.; Randall, C. A.; Levin, I. *J. Appl. Phys.* **2004**, *96* (5), 2828–2831.
(39) Shoto, K.; Eisuke, M.; Chikako, M.; Yoshihiro,

K.; Nao, T.; Hiroshi, T.; Sachiko, M.; Masaki, T.; Satoshi, W. *Jpn. J. Appl. Phys.* **2013**, *52* (9S1), 09KF04.
(40) Malibert, C.; Dkhil, B.; Kiat, J. M.; Durand, D.; Berar, J. F.; Spasojevic de Bire, A. *J. Phys. Condens. Matter* **1997**, *9*, 7485–7500.
(41) Dolgos, M.; Adem, U.; Wan, X.; Xu, Z.; Bell, A. J.; Comyn, T. P.; Stevenson, T.; Bennett, J.; Claridge, J. B.; Rosseinsky, M. J. *Chem. Sci.* **2012**, *3* (5), 1426–1435.
(42) Perrin, C.; Menguy, N.; Suard, E.; Muller, C.; Caranoni, C.; Stepanov, A. *J. Phys. Condens. Matter* **2000**, *12*, 7523–7539.
(43) Itoh, K.; Zeng, L. Z.; Nakamura, E.; Mishima, N. *Ferroelectrics* **1985**.
(44) Bonneau, P.; Garnier, P.; Husson, E.; Morell, A. *Mater. Res. Bull.* **1989**, *24* (2), 201–206.
(45) Uesu, Y.; Tazawa, H.; Fujishiro, K.; Yamada, Y. *J. Korean Phys. Soc.* **1996**, *29*, S703–S705.
(46) Johnston, K. E.; Tang, C. C.; Parker, J. E.; Knight, K. S.; Lightfoot, P.; Ashbrook, S. E. *J. Am. Chem. Soc.* **2010**, *132* (25), 8732–8746.
(47) Darlington, C. N. W.; Knight, K. S. *Acta Crystallogr. Sect. B Struct. Sci.* **1999**, *55* (1), 24–30.
(48) Solov'ev, S. P.; Venevtsev, Y. N.; Zhdanov, G. S. *Sov. Phys. - Crystallogr.* **1961**, *6* (2), 171–175.
(49) Tellier, J.; Malic, B.; Dkhil, B.; Jenko, D.; Cilensek, J.; Kosec, M. *Solid State Sci.* **2009**, *11* (2), 320–324.
(50) Ogihara, H.; Randall, C. A.; Trolier-McKinstry, S. *J. Am. Ceram. Soc.* **2009**, *92* (1), 110–118.
(51) Sun, X.; Chen, J.; Yu, R.; Sun, C.; Liu, G.; Xing, X.; Qiao, L. *J. Am. Ceram. Soc.* **2009**, *92* (1), 130–132.
(52) Manjón-Sanz, A.; Berger, C.; Dolgos, M. R. *J. Mater. Sci.* **2017**, *52* (9), 5309–5323.
(53) Krayzman, V.; Levin, I.; Woicik, J. C.; Bridges, F. *Appl. Phys. Lett.* **2015**, *107* (19), 7–12.
(54) Mitchell, R. H.; Burns, P. C.; Knight, K. S.; Howard, C. J.; Chakhmouradian, A. R. *Phys. Chem. Miner.* **2014**, *41* (6), 393–401.
(55) Shanker, V.; Samal, S. L.; Pradhan, G. K.; Narayana, C.; Ganguli, A. K. *Solid State Sci.* **2009**, *11* (2), 562–569.
(56) Chaker, C.; El Gharbi, W.; Abdelmoula, N.; Simon, A.; Khemakhem, H.; Maglione, M. *J. Phys. Chem. Solids* **2011**, *72* (10), 1140–1146.
(57) Schulze, W. A.; Seth, V. K. *Ultrason. Ferroelectr. Freq. Control. IEEE Trans.* **1989**, *36* (8824326), 41–49.
(58) Yan, H.; Zhang, H.; Ubic, R.; Reece, M.; Liu, J.; Shen, Z. *J. Mater. Sci. Mater. Electron.* **2006**, *17* (9), 657–661.
(59) Guo, J.; Guo, H.; Baker, A. L.; Lanagan, M. T.; Kupp, E. R.; Messing, G. L.; Randall, C. A. *Angew. Chemie - Int. Ed.* **2016**, *55* (38), 11457–11461.